THE JOURNAL OF PHYSICAL CHEMISTRY C

ARTICLE

pubs.acs.org/JPCC

First-Principles Study of Electron Mobility in Cationic and Anionic Conjugated Polyelectrolytes

Zi Li,[†] Xu Zhang,[†] Gang Lu,[*,†] and Thuc-Quyen Nguyen[‡]

[†]Department of Physics and Astronomy, California State University Northridge, Northridge, California 91330, United States

[‡]Department of Chemistry and Biochemistry, University of California, Santa Barbara, California 93106, United States

ABSTRACT: Electron mobilities in two similar conjugated polyelectrolytes (CPEs) with an identical conjugated backbone but different counterions and appended charges are calculated from first-principles. An excellent agreement with experimental mobility is found for the cationic CPE. The relative importance and respective role of CPE structural components including backbone, appended groups, and counterions in determining electron mobility are examined in detail. Experimentally observed large electron mobility difference between the cationic and anionic CPEs is understood and attributed to the energetic disorder, which in turn is determined by the dynamics of the counterions. The energy alignment between the electrode and the CPEs is found to be crucially important for the experimental measurements leading to mobilities. For similar backbone and counterions, a cationic CPE is predicted to have a higher intrinsic carrier mobility than an anionic CPE in general.

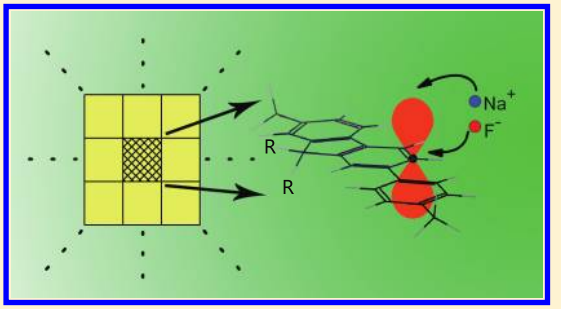

INTRODUCTION

Conjugated polyelectrolytes (CPEs) are polymers comprised of π-conjugated backbones and ionic functional groups. The delocalized π states of the backbones endow a CPE with desirable optoelectronic properties, characteristic of semiconducting polymers, while the ionic functional groups impart the CPE with solubility in and the ability to process from aqueous solutions, characteristic of traditional polyelectrolytes.[1−4] Widely regarded as one of the most interesting and useful classes of conjugated polymers,[2] CPEs have found applications in light-emitting diodes,[5−7] photovoltaic devices,[8,9] photodetectors and chemical/biological sensors,[3,10,11] etc. It has also been recognized that carrier mobility plays a crucial if not dominant role in the performance of the CPE devices. However, hitherto the charge transport mechanism in CPEs remains largely unknown. In particular, although various structural components of CPEs, including the conjugated backbone,[7] counterion,[12,13] and appended ionic group,[7,14] have been found to influence carrier mobility, their relative importance and respective role in determining carrier mobility are poorly understood. The lack of fundamental understanding in CPEs represents a major roadblock to further improve their performance, and thus theoretical studies of CPEs are in critical demand. In this Article, we carry out first-principles simulations to examine the respective roles of the structural components and assess their relative importance in controlling carrier mobility. Specifically, we focus on a recent experimental observation that two similar CPEs with an identical conjugated backbone but different counterions and appended charge groups exhibit 4 orders of magnitude difference in electron mobility.[14] The origin of the contrasting mobilities in the two CPEs is elucidated by the first-principles simulations, which shed light into the underlying electron transport mechanism. To the best of our knowledge, the present work represents the first theoretical/computational effort to study carrier mobility in CPEs that is based on first-principles with no empirical input or adjustable parameters.

In the recent experiment by Garcia et al.,[14] the electron mobility in a cationic CPE, poly[(9,9-bis(6′-(*N*,*N*,*N*-trimethylammonium) hexyl))-fluorene-*alt*-*co*-1,4-phenylene] fluoride (PFNF), and an anionic CPE, sodium poly[9,9-bis(5′-pentanoate)fluorene-*alt*-*co*-1,4-phenylene] ($PFCO_2Na$), was measured using electron-only diodes with Al and Ba electrodes. The backbone of the two CPEs is identical, and the only structural differences between them are the appended charge groups and the counterions $-N(CH_3)_3^+$ group and F^- ion for PFNF, and $-CO_2^-$ group and Na^+ ion for $PFCO_2Na$. Despite the structural similarity, the measured zero-field electron mobility is 5.3×10^{-4} $cm^2/(V\ s)$ for PFNF and 1.1×10^{-8} $cm^2/(V\ s)$ $PFCO_2Na$, with 4 orders of magnitude difference between them. Because carrier mobility in CPEs is often associated with the properties of the semiconducting backbones, this result appears beyond the conventional wisdom, which motivates the present theoretical investigation.

THEORETICAL FRAMEWORK AND COMPUTATIONAL DETAILS

The theoretical framework is based on an ab initio multiscale approach,[15,16] which combines ab initio Born−Oppenheimer molecular dynamics (BOMD), ab initio nonadiabatic molecular dynamics (NAMD),[17] and a solution of static master equations

Received: August 24, 2011
Published: December 09, 2011

for a macroscopic system. The macroscopic system is divided into 100 × 100 × 100 cubes for which the carrier mobility is calculated (Figure 1). The BOMD is performed on one of the 10^6 cubes, named the home cube; the electronic wave functions (and energies) in the home cube are then used to generate the wave functions (and energy disorder) in the other cubes. More specifically, the wave functions (and their energies) in each cube are selected from those in the home cube at a random MD snapshot and then randomly rotated before placing in each cube. This is an approximate scheme to generate a random wave function network for a disordered system. The justification and validation of the scheme can be found in previous work.[15] The NAMD is subsequently carried out for the home cube to determine the transition rates between these wave functions. The NAMD captures phonon-assisted electron or hole transitions between localized electronic states in disordered semiconducting polymers. Finally, on the basis of the transition rates, the static master equations are solved on the macroscopic system to calculate the carrier mobility. In the following, we provide a detailed description of the theoretical framework and computational parameters.

Ab Initio BOMD Simulation. The ab initio BOMD simulation is performed for the home cube with the standard plane-wave pseudopotential approach and the generalized gradient approximation[18] as implemented in the VASP code.[19,20] The calculation is performed at the gamma point only (at the center of the Brillouin zone), and the energy cutoff of the plane-wave basis is 400 eV. The lattice constant of the home cube is 16.54 Å, and the cube contains three polymer chains, each with two backbone segments as shown in Figure 1. There are 390 and 582 atoms in the home cube, corresponding to a mass density of 1.1 and 1.3 g/cm^3 for $PFCO_2Na$ and PFNF, respectively, close to the experimental density.[21] In general, the dimensions of the home cube should be chosen as large as computationally feasible, but the minimal dimensions of the cube should be greater than the intersite distance defined in Gaussian Disordered Model (GDM),[22] which is about 16 Å for the conjugated polymers.[23] The wave functions of the two lowest conduction bands of $PFCO_2Na$ are presented in Figure 1, which are localized in the home cube, and thus the position of the carrier can be estimated from the wave functions. The wave functions are localized because they are not continuous throughout the entire system, and thus the random rotations of them in the neighboring cubes will generate a discontinuous/localized wave function network for the entire system.

To construct a disordered system, we first placed three polymer chains in a large simulation cell, and then performed classical isothermal−isobaric (NPT) MD at 1000 K to obtain a disordered structure with a lattice constant of 16.54 Å, which was the initial configuration for the subsequent first-principles simulations. The disordered initial structure was then fully relaxed by a static first-principles calculation to reach the local equilibrium, and the ab initio BOMD simulation was followed to bring the system to 300 K with repeated velocity scalings; the system was kept at 300 K for 500 fs to reach the thermal equilibrium. Finally, a microcanonical BOMD production run was carried out for 3000 fs. In all of the BOMD simulations, the time-step was 1 fs.

NAMD for Transition Rates. On the basis of the Kohn−Sham (KS) wave functions and energies at different MD time-steps, we can calculate the phonon-assisted transition rates between these KS states in the home cube; these transition rates are obtained from the NAMD simulations of the home cube,[15] and they are called intracube transition rates in the following. We expand the time-dependent one-electron wave function of the carrier,

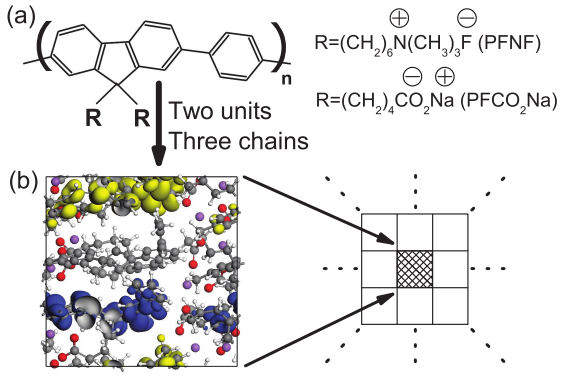

Figure 1. (a) Schematic diagram of the CPEs backbone; "R" represents the side chain $-(CH_2)_6N(CH_3)_3$ in PFNF and $-(CH_2)_4CO_2Na$ in $PFCO_2Na$, respectively. (b) Atomic structure of $PFCO_2Na$ in the home cube; the wave functions of the two lowest conduction bands are shown with two isosurfaces (blue and yellow). The gray, white, red, and purple colors represent carbon, hydrogen, oxygen, and sodium atoms, respectively. The entire system consists of 100 × 100 × 100 cubes.

$\psi^{(i)}(\mathbf{r},t)$, in terms of a full set of adiabatic KS orbitals $\phi_j(\mathbf{r},\mathbf{R}(t))$:

$$\psi^{(i)}(\mathbf{r},t) = \sum_j c_j^{(i)}(t)\phi_j(\mathbf{r},\mathbf{R}(t)) \quad (1)$$

Here, $\phi_j(\mathbf{r},\mathbf{R}(t))$ is the jth eigenstate of the KS Hamiltonian for the current ionic position $R(t)$, and $c_j^{(i)}(t)$ is the corresponding expansion coefficient. The superscript i signifies that at $t = 0$, $\psi^{(i)}(\mathbf{r},0) = \phi_i(\mathbf{r},\mathbf{R}(0))$ is an initial condition. For simplicity, we assume that at $t = 0$, the carrier is in a pure state $\phi_i(\mathbf{r},\mathbf{R}(0))$, and the subsequent motion of ions evolves the state to a mixed state as in eq 1. The expansion coefficient thus represents the transition probability amplitude from the initial state i to the state j. These transitions are made possible by the ionic motion, and thus the transitions are called phonon-assisted transitions. Substituting eq 1 into the time-dependent KS equation, one can obtain the following equation for the evolution of the coefficient $c_j^{(i)}(t)$:[17]

$$\frac{\partial}{\partial t}c_j^{(i)}(t) = -\sum_k c_k^{(i)}(t)\left(\frac{i}{\hbar}\varepsilon_k\delta_{jk} + d_{jk}\right) \quad (2)$$

where ε_k is the energy of the kth KS orbital, and d_{jk} is the nonadiabatic coupling (NAC) between the jth and kth KS orbitals:

$$d_{jk} \equiv \langle\phi_j|\nabla_{\mathbf{R}}|\phi_k\rangle\cdot\frac{\mathrm{d}\mathbf{R}}{\mathrm{d}t} = \left\langle\phi_j\middle|\frac{\partial}{\partial t}\middle|\phi_k\right\rangle \quad (3)$$

Equation 2 is propagated over a 100 fs-long trajectory with an initial condition $c_j^{(i)}(t=0) = \delta_{ij}$ imposed at each BOMD time-step; the eigenvalues and NAC at each BOMD time-step are used in the propagation of eq 2. Because the carriers are conduction electrons in these CPEs, the indices i and j represent conduction bands only; the 18 lowest conduction bands spreading over 1.2 eV are considered in the simulations.

The electron transition (ET) dynamics from state i to state j can be expressed as $\mathrm{ET}(t) = 1 - \exp(t/\tau)$, where $\mathrm{ET}(t) = |c_j^{(i)}(t)|^2$ is the electron transfer amount from the state i to the state j at time t. τ is the characteristic time scale for the electron transfer, and $1/\tau$ is thus the transition rate. The equation is valid as long as the system is thermal equilibrium. An NAMD trajectory of 100 fs is used to fit to the equation from which the characteristic transition time scale or rate can be estimated

at each BOMD time-step. Thus, 3000 such trajectories are obtained to determine the transition rates at all BOMD time-steps. Because t is less than 100 fs while $\tau \approx 10^5$ fs (cf., Figure 2b), one can approximate the exponential by a linear equation $\mathrm{ET}(t) \approx t/\tau$, and thus the transition rate γ_{ij}^0 can be estimated as

$$\gamma_{ij}^0 = \langle |c_j^{(i)}(t)|^2/t \rangle \tag{4}$$

where $\langle ... \rangle$ indicates an average taken over the 100 fs NAMD trajectory.

In the macroscopic system consisting of 100 × 100 × 100 cubes, one can determine the intercube transition rate $\gamma_{ij'}^0$ between state i in cube n and state j' in the adjacent cube m from the relevant intracube transition rates as:[15,24]

$$\gamma_{ij'}^0 = (\gamma_{ij}^0 + \gamma_{i'j'}^0)/2 \tag{5}$$

where the states i' and j are selected from the cube n and m, respectively, so that the distances R_{ij} and $R_{i'j'}$ match as closely as possible to $R_{ij'}$. Because the states i and j (i' and j') fall within the same cube n (m), their intracube transition rates are calculated by eq 4. Finally, to ensure a detailed balance for the uphill energetic transitions, that is, $\varepsilon_{j'} \geq \varepsilon_i$ (the electrons have to adsorb phonons from the thermal equilibrated system), the thermal equilibrium transition rate $\gamma_{ij'}$ is defined as[25]

$$\gamma_{ij'} = \begin{cases} \gamma_{ij'}^0 \exp\left(-\dfrac{\varepsilon_{j'} - \varepsilon_i - eER_{n,m}^x}{k_B T}\right), & \text{if } \varepsilon_{j'} \geq \varepsilon_i + eER_{n,m}^x \\ \gamma_{ij'}^0, & \text{if } \varepsilon_{j'} < \varepsilon_i + eER_{n,m}^x \end{cases} \tag{6}$$

Here, ε_i and $\varepsilon_{j'}$ are the energies of the states i and j' in the cube n and m, respectively. The term $-eER_{n,m}^x$ represents the energy shift in the presence of a uniformly applied electric field E in the x direction; $R_{n,m}^x$ is the distance between the cube n and m in the x direction.

Master Equation for Mobility. The carrier mobility is calculated on the macroscopic system by solving the static master equation for each cube n in equilibrium, that is:

$$\sum_m [\Gamma_{n\to m} - \Gamma_{m\to n}] = 0 \tag{7}$$

Here, $\Gamma_{n\to m}$ is the macroscopic transition rate for the charge carrier from cube n to cube m, summing up all intercube transition rates:

$$\Gamma_{n\to m} = \sum_{i\in n} p_n f_i \sum_{j'\in m} \gamma_{i,j'}(1 - p_m f_{j'}) \tag{8}$$

where the summations of i and j' are over all relevant electronic states of the carrier in the cube n and m, respectively; p_n is the partial concentration or density of the carriers in the cube n, and f_i is the Fermi–Dirac occupation of the state i. Note that the carrier concentration p_n is unknown and needs to be determined by self-consistently solving the master equations.[26] With the macroscopic transition rates $\Gamma_{n\to m}$, the carrier mobility μ is given by

$$\mu = \frac{\sum_{n,m} \Gamma_{n\to m} R_{n,m}^x}{pEV} \tag{9}$$

where p is the total carrier concentration and V is the volume of the entire system. In this work, we set $p = 10^{-6}$/cube, corresponding to an electron concentration of $2 \times 10^{14}\mathrm{cm}^{-3}$, which is a typical value used in experiments.[27]

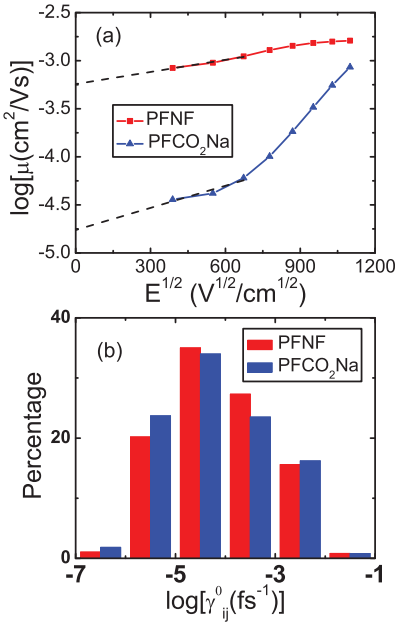

Figure 2. (a) Electron mobility of PFNF (red) and $PFCO_2Na$ (blue) versus the squared root of the applied uniform electric field at 300 K. The dash lines are the linear fits to the simulated mobility in the region of $(E)^{1/2} < 700\ (\mathrm{V/cm})^{1/2}$. (b) Percentage distribution of the logarithm of the interstate transition rates $\log[\gamma_{ij}^0]$ of PFNF (red) and $PFCO_2Na$ (blue).

RESULTS AND DISCUSSION

The calculated electron mobility as a function of applied uniform electric field is displayed in Figure 2a. We found that the mobility follows approximately the well-known Poole–Frenkel form, that is, $\mu \propto \exp(\gamma(T)(E)^{1/2})$, over an extended range of the electric fields;[28−30] here, $\gamma(T)$ is the field activation factor. The minor deviation from the Poole–Frenkel form at low E fields has also been observed in the experiment[14] and predicted by the GDM.[22] The mobility at zero E field is determined by a linear fit to the computational data in the range of $((E)^{1/2}) < 700\ (\mathrm{V/cm})^{1/2}$, and the corresponding mobility is $5.7 \times 10^{-4}\ \mathrm{cm}^2/(\mathrm{V\ s})$ for PFNF and $1.7 \times 10^{-5}\ \mathrm{cm}^2/(\mathrm{V\ s})$ for $PFCO_2Na$. The first-principles determined zero-field mobility for PFNF is in an excellent agreement with the experimental value of $5.3 \times 10^{-4}\ \mathrm{cm}^2/(\mathrm{V\ s})$, while the theoretical mobility for $PFCO_2Na$ is much higher than the experimental value of $1.1 \times 10^{-8}\ \mathrm{cm}^2/(\mathrm{V\ s})$. In the remainder of this Article, we will first understand the contrasting mobilities between the two CPEs and then address the discrepancy between the theoretical and experimental mobilities for $PFCO_2Na$.

It is well established that the carrier mobility is proportional to the thermal equilibrium transition rates,[15] which according to eq 6 can be affected by two factors. They are the intrinsic transition rate $\gamma_{ij'}^0$ and the energy difference between two relevant states where a transition takes place. The percentage distributions of γ_{ij}^0 for the two CPEs are shown in Figure 2b, indicating rather similar distributions of the transition rates. PFNF has slightly larger intrinsic transition rates than $PFCO_2Na$. This result is not surprising because the two CPEs share the same backbone

dx.doi.org/10.1021/jp210751a | J. Phys. Chem. C 2012, 116, 1205–1210

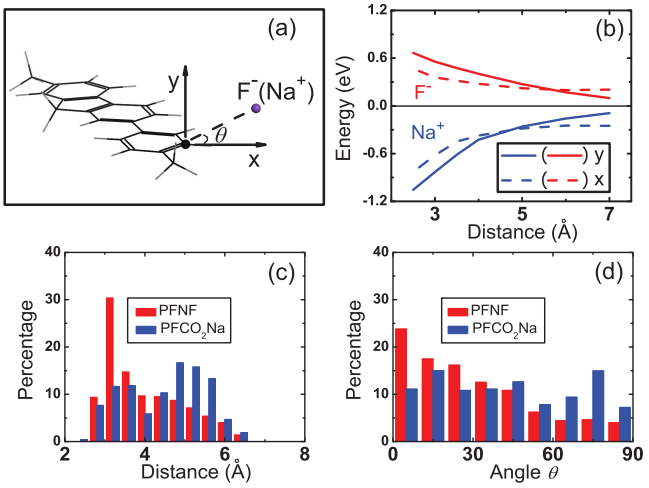

Figure 3. (a) Model used in the simulations for ionic dynamics. The origin is placed at a backbone carbon atom that is closest to the ions. y axis is perpendicular to the backbone plane,and x axis is in the backbone plane. (b) LUMO energy as a function of the distance between the origin and the ion in x (dash) and y (solid) directions; the red (blue) curves correspond to the F^- (Na^+) ion. The LUMO energy of the system in the absence of ions is set to be zero. (c) Percentage distribution of the distance between the ion and the origin determined from the ionic dynamics. (d) Percentage distribution of the angle θ determined from the ionic dynamics.

structure. Therefore, we conclude that the intrinsic transition rates are determined by the π-conjugated backbone of the CPEs. However, it turns out that the energy difference or the energetic disorder in the two CPEs is very different, stemming from the different dynamic behaviors of the counterions. Because the LUMO level has the greatest contribution to the carrier mobility among all conduction states thanks to the Fermi−Dirac statistics, we represent the energetic disorder of the system by the standard deviation of the LUMO energy:

$$\Delta E^2 = \sum_{i=1}^{N} (E_i - \overline{E})^2 / N \qquad (10)$$

Here, E_i is the LUMO energy at a time-step i along the BOMD trajectory, $\overline{E}$ is the average energy of E_i over the course of the BOMD, and $N = 3000$ is the total number of BOMD time-steps. Because the wave functions and energies of the MD snapshots are randomly placed in the macroscopic system, the energy fluctuation of the BOMD reflects a measure of the static disorder in the system. We have calculated the standard deviation for the LUMO level of PFNF as 0.077 eV and of $PFCO_2Na$ as 0.103 eV. The corresponding experimental values fitted to the GDM model are 0.087 eV for PFNF and 0.116 eV for $PFCO_2Na$, respectively,[14] which agree very well with the theoretical results. Because the equilibrium transition rates depend exponentially on the energetic disorder, the moderately wider energy distribution (or more energetic disorder) in $PFCO_2Na$ could lead to a much lower carrier mobility, confirmed by both theory and experiment.

In the following, we examine whether the different LUMO energy distributions are indeed caused by the dynamics of the counterions. To this end, we consider a simplified model, which captures the essential physics. In this model, only one repeated unit of the backbone is considered, and the LUMO energy of the backbone is calculated as a function of the displacement between

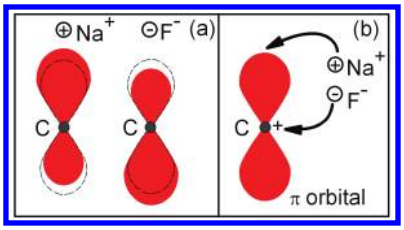

Figure 4. Schematic picture for the interaction between the ions and the π orbital. The red region indicates the electron distribution of the π orbital. (a) Opposite π orbital polarizations due to the presence of the ions; the dash contour represents the original π orbital before the polarization. (b) F^- ions prefer to move along the x direction.

the ion (either F^- or Na^+) and the origin in x and y directions (Figure 3). The LUMO level consists of conjugated π states on the backbone carbon atoms, and, at the origin, the π charge density is oriented along the y direction; thus, as the x and y distances increase, the Coulomb energy between the F^- ion and the π electrons decreases, and hence the LUMO energy decreases as is well shown in Figure 3b. On the contrary, the LUMO energy increases as the Na^+ ion moves away from the origin. Moreover, as the displacement changes from 3 to 7 Å, the energy increase of Na^+ exceeds the energy decrease of F^- as shown in Figure 3b. This is because the two ions produce the opposite charge polarizations as depicted in Figure 4a; the polarization due to the Na^+ ion yields a greater energy change as compared to that due to the F^- ion. This result is general and has an important consequence in the energetic disorder of CPEs as discussed in the following. Finally, the energy variation along the y axis is more than that along the x axis for both types of ions because the π orbital is along the y direction.

From the BOMD trajectory, one can determine the statistics of ionic dynamics. The percentage distribution for the distance between the ions and their nearest carbon atoms on the backbone is shown in Figure 3c. One finds that the F^- ions in PFNF have a rather narrow distribution, peaked at 3 Å. On the other hand, the Na^+ ions in $PFCO_2Na$ have a much broader distance distribution. This difference may be attributed to the fact that the radius of the F^- ion (1.33 Å) is larger than that of the Na^+ ion (1.02 Å). The angle distribution of the two CPEs is shown in Figure 3d, and the angle θ is labeled in Figure 3a. It is observed again that the F^- ions in PFNF have a narrower distribution, with a peak at some small angles. In contrast, the Na^+ ions in $PFCO_2Na$ display a broader and a more uniform distribution of angles. Hence, the F^- ions move primarily along the x direction indicated by the nature of the π orbitals (cf., Figure 4b), while the Na^+ ions are more uniformly distributed. From the results, three observations are in order: (1) the LUMO energy variation is less in magnitude in PFNF than in $PFCO_2Na$ for the distances covered in Figure 3b; (2) the F^- ions are mostly distributed along the nodal plane (or in the x direction) of the π orbitals, which renders to a smaller energy variation than in other directions; and (3) the smaller distance fluctuation of the F^- ions leads to a smaller LUMO energy variation. Therefore, we conclude that the ionic dynamics in PFNF results in a smaller LUMO energy variation or less energetic disorder, which in turn yields a higher electron mobility. In fact, the first two observations should be generally valid in comparisons between cationic and anionic CPEs with similar backbone and counterions.

The mobility discrepancy in $PFCO_2Na$ between the theory and the experiment is attributed to the electrode contact.

The theoretical calculation probes the intrinsic electron mobility, while the experiment measures the overall mobility, including the extrinsic factors such as the electrode contact resistance. It turns out that the significantly lower overall mobility from the experiment actually results from the energy misalignment between the Fermi level of the electrode and the LUMO level of $PFCO_2Na$. We have carried out first-principles calculations for the electrode/CPE interfaces, focusing on the energy level alignment. The Ba electrode used in the experiment as cathode is modeled here. Both $PFCO_2Na$ and PFNF are considered, and the backbone of the CPEs is parallel to the Ba (100) surface. Two backbone−surface distances are studied: 5 and 11 Å. It is found the LUMO level of both CPEs is higher than the Ba Fermi energy for both distances, which is consistent with the experimental estimate.[14] More importantly, the energy difference between the LUMO and the Fermi level is 0.03 eV for PFNF and 0.17 eV for $PFCO_2Na$ at the distance of 5 Å. This energy disparity increases to 0.1 eV for PFNF and 0.32 eV for $PFCO_2Na$ at the distance of 11 Å. Therefore, there is an energy barrier for the electrons to be injected from the electrode to the CPEs at the distance of 5 Å; this energy barrier is much higher (5−6 times higher) for $PFCO_2Na$ than for PFNF. The same trend holds even if the CPEs are far away from the Ba surface at 11 Å. In other words, the energy level misalignment between Ba and $PFCO_2Na$ is intrinsic, not due to CPE−metal interactions. The much smaller energy barrier in PFNF renders the overall mobility to be close to the intrinsic mobility; hence, the comparison between the theory and the experiment is excellent. On the other hand, the much higher energy barrier in $PFCO_2Na$ causes the overall mobility to be much lower than the intrinsic mobility; thus, the experimental value is much lower than the theoretical one. Our finding is also consistent with a previous experimental result for the similar CPEs on a gold surface,[31] which also showed that the cationic CPE has a smaller electron injection energy barrier than the anionic CPE. The reason is that on average the charge groups are farther in distance from the backbone than the counterions are from the backbone, and therefore the cationic group decreases the LUMO energy of the backbone (the cationic group and the negative counterions in the same CPE have the opposite effect on the LUMO level, but the cationic group wins because it is closer to the backbone), while the anionic group increases the LUMO energy of the backbone (the anionic group increases the LUMO energy, while the positive counterions lower the LUMO energy, but the anionic group prevails). Hence, the LUMO level of the anionic CPE is elevated further above the Fermi energy (or the work-function) of the electrode, leading to a higher ejection energy barrier as observed above.

SUMMARY

We have calculated electron mobilities in two CPEs by a first-principles method. An excellent agreement with the experimental mobility is obtained for the cationic CPE. The theoretical investigations shed light into the respective roles of the CPE components on the electron mobility. We find that the counterions can affect the energetic disorder, which in turn can influence the carrier mobility by 1 or 2 orders of magnitude for the CPEs studied here. The appended charge groups, on the other hand, mainly affect the position of the LUMO level, and thus influence the ejection energy barrier from the electrode. On the basis of the comparison between the theoretical and the experimental mobilities in $PFCO_2Na$, we find that the effect of the appended groups on the mobility could be significant, up to 3 orders of magnitude. The backbone primarily controls the electron transition rates, which are proportional to the carrier mobility. Because the carrier mobility depends exponentially on the energy fluctuation, one would expect that the backbone has a smaller effect on mobility as compared to the counterions. It appears that with similar backbone and counterions, a cationic CPE should in general have a higher intrinsic carrier mobility than an anionic CPE. Finally, we emphasize that the energetic alignment between CPEs and electrodes is an important factor in interpreting experimental carrier mobilities.

AUTHOR INFORMATION

Corresponding Author
*E-mail: ganglu@csun.edu.

ACKNOWLEDGMENT

This work was supported by NSF Solar energy grant DMR-1035480. The computational facility is provided by the Army High Performance Computing Research Center and NSF MRI-R^2 grant DMR-0958596.

REFERENCES

(1) Hoven, C. V.; Garcia, A.; Bazan, G. C.; Nguyen, T. Q. *Adv. Mater.* **2008**, *20*, 3793–3810.
(2) Jiang, H.; Taranekar, P.; Reynolds, J. R.; Schanze, K. S. *Angew. Chem., Int. Ed.* **2009**, *48*, 4300–4316.
(3) Thomas, S. W.; Joly, G. D.; Swager, T. M. *Chem. Rev.* **2007**, *107*, 1339–1386.
(4) Ho, H. A.; Najari, A.; Leclerc, M. *Acc. Chem. Res.* **2008**, *41*, 168–178.
(5) Edman, L.; Pauchard, M.; Liu, B.; Bazan, G.; Moses, D.; Heeger, A. J. *Appl. Phys. Lett.* **2003**, *82*, 3961–3963.
(6) Wu, H. B.; Huang, F.; Mo, Y. Q.; Yang, W.; Wang, D. L.; Peng, J. B.; Cao, Y. *Adv. Mater.* **2004**, *16*, 1826.
(7) Garcia, A.; Yang, R.; Jin, Y.; Walker, B.; Nguyen, T. Q. *Appl. Phys. Lett.* **2007**, *91*, 153502.
(8) Mwaura, J. K.; Pinto, M. R.; Witker, D.; Ananthakrishnan, N.; Schanze, K. S.; Reynolds, J. R. *Langmuir* **2005**, *21*, 10119–10126.
(9) Taranekar, P.; Qiao, Q.; Jiang, H.; Ghiviriga, I.; Schanze, K. S.; Reynolds, J. R. *J. Am. Chem. Soc.* **2007**, *129*, 8958.
(10) Gaylord, B. S.; Heeger, A. J.; Bazan, G. C. *Proc. Natl. Acad. Sci. U.S.A.* **2002**, *99*, 10954–10957.
(11) Liu, B.; Bazan, G. C. *Chem. Mater.* **2004**, *16*, 4467–4476.
(12) Yang, R. Q.; Garcia, A.; Korystov, D.; Mikhailovsky, A.; Bazan, G. C.; Nguyen, T. Q. *J. Am. Chem. Soc.* **2006**, *128*, 16532–16539.
(13) Garcia, A.; Nguyen, T. Q. *J. Phys. Chem. C* **2008**, *112*, 7054–7061.
(14) Garcia, A.; Jin, Y.; Brzezinski, J. Z.; Nguyen, T. Q. *J. Phys. Chem. C* **2010**, *114*, 22309–22315.
(15) Zhang, X.; Li, Z.; Lu, G. *Phys. Rev. B* **2010**, *82*, 205210.
(16) Li, Z.; Zhang, X.; Lu, G. *Comput. Phys. Commun.* **2011**, *182*, 2632–2637.
(17) Duncan, W. R.; Stier, W. M.; Prezhdo, O. V. *J. Am. Chem. Soc.* **2005**, *127*, 7941–7951.
(18) Perdew, J. P.; Burke, K.; Ernzerhof, M. *Phys. Rev. Lett.* **1996**, *77*, 3865.
(19) Kresse, G.; Hafner, J. *Phys. Rev. B* **1993**, *47*, 558–561.
(20) Kresse, G.; Furthmuller, J. *Phys. Rev. B* **1996**, *54*, 11169–11186.
(21) Mardalen, J.; Samuelsen, E. J.; Gautun, O. R.; Carlsen, P. H. *Solid State Commun.* **1991**, *77*, 337–339.
(22) Bassler, H. *Phys. Status Solidi B* **1993**, *175*, 15–56.

(23) Pasveer, W. F.; Cottaar, J.; Tanase, C.; Coehoorn, R.; Bobbert, P. A.; Blom, P. W. M.; de Leeuw, D. M.; Michels, M. A. J. *Phys. Rev. Lett.* **2005**, *94*, 206601.
(24) Vukmirovic, N.; Wang, L. W. *Nano Lett.* **2009**, *9*, 3996–4000.
(25) Duncan, W. R.; Craig, C. F.; Prezhdo, O. V. *J. Am. Chem. Soc.* **2007**, *129*, 8528–8543.
(26) Yu, Z. G.; Smith, D. L.; Saxena, A.; Martin, R. L.; Bishop, A. R. *Phys. Rev. B* **2001**, *63*, 085202.
(27) Tanase, C.; Meijer, E. J.; Blom, P. W. M.; de Leeuw, D. M. *Phys. Rev. Lett.* **2003**, *91*, 216601.
(28) Abkowitz, M.; Bassler, H.; Stolka, M. *Philos. Mag. B* **1991**, *63*, 201–220.
(29) Blom, P. W. M.; deJong, M. J. M.; vanMunster, M. G. *Phys. Rev. B* **1997**, *55*, R656–R659.
(30) Campbell, I. H.; Smith, D. L.; Neef, C. J.; Ferraris, J. P. *Appl. Phys. Lett.* **1999**, *74*, 2809–2811.
(31) Seo, J. H.; Yang, R. Q.; Brzezinski, J. Z.; Walker, B.; Bazan, G. C.; Nguyen, T. Q. *Adv. Mater.* **2009**, *21*, 1006–1011.